Provided for non-commercial research and education use.
Not for reproduction, distribution or commercial use.

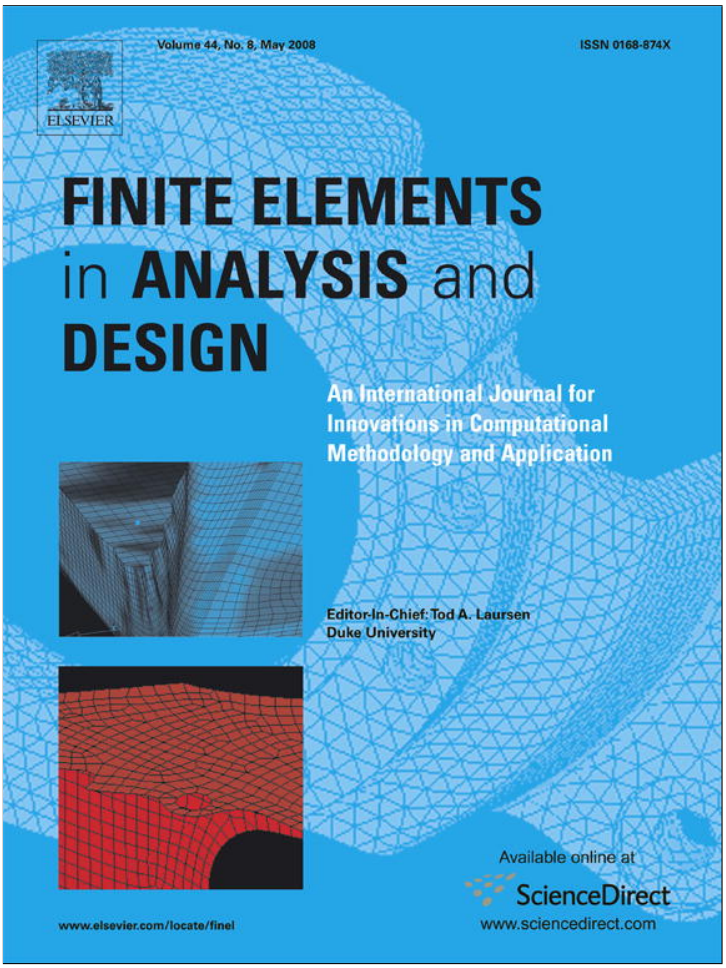

This article appeared in a journal published by Elsevier. The attached copy is furnished to the author for internal non-commercial research and education use, including for instruction at the authors institution and sharing with colleagues.

Other uses, including reproduction and distribution, or selling or licensing copies, or posting to personal, institutional or third party websites are prohibited.

In most cases authors are permitted to post their version of the article (e.g. in Word or Tex form) to their personal website or institutional repository. Authors requiring further information regarding Elsevier's archiving and manuscript policies are encouraged to visit:

http://www.elsevier.com/copyright

Author's personal copy

Available online at www.sciencedirect.com
ScienceDirect
Finite Elements in Analysis and Design 44 (2008) 439–449
FINITE ELEMENTS IN ANALYSIS AND DESIGN
www.elsevier.com/locate/finel

Topology optimization of periodic Mindlin plates

Adel El-Sabbagh[a], Wael Akl[a], Amr Baz[b,*]

[a]*Design and Production Engineering Department, Faculty of Engineering, Ain Shams University, Cairo, Egypt*
[b]*Mechanical Engineering Department, University of Maryland, College Park, MD 20742, USA*

Received 24 July 2007; received in revised form 4 January 2008; accepted 5 January 2008
Available online 6 March 2008

Abstract

Periodic structures exhibit unique dynamic characteristics that make them act as tunable mechanical filters for wave propagation. As a result, waves can propagate along the periodic structures only within specific frequency bands called the 'pass bands' and wave propagation is completely blocked within other frequency bands called the 'stop bands' or 'band gaps'. The spectral width of these bands can be optimized using topology optimization. In this paper, topology optimization is used to maximize the fundamental natural frequency of Mindlin plates while enforcing periodicity. A finite element model for Mindlin plates is presented and used along with an optimization algorithm that accounts for the periodicity constraint in order to determine the optimal topologies of plates with various periodic configurations. The obtained results demonstrate the effectiveness of the proposed design optimization approach in generating periodic plates with optimal natural frequency and wide stop bands. The presented approach can be invaluable design tool for many structures in order to control the wave propagation in an attempt to stop/confine the propagation of undesirable disturbances.
© 2008 Elsevier B.V. All rights reserved.

Keywords: Topology optimization; Periodic structures; Mindlin plates; Stop bands

1. Introduction

Topology optimization has been extensively applied to a wide variety of structures in order to optimize their static and dynamic characteristics. For instance, topology optimization was employed to minimize the compliance of plates subject to in-plane single load [1] and multiple loads [2]. Also, topology optimization has been used to maximize the eigen-frequencies of the lateral vibration of plates [3,4] and the buckling stiffness of cylindrical shells with inner-wall stiffeners [5]. Other attempts include optimization of the structural topologies for power flow distribution [6] and energy absorption characteristics of multi-material structures [7].

Recently, the emphasis is placed on maximizing the stop bands (or band gaps) of various types of periodic structures. For example, Sigmund and Jensen [8] optimized the topology of sonic band gap structures subject to periodic loading and Diáz et al. [9] optimized the band gap properties of grillage structures. Also, Halkjaer et al. [10,11] maximized the band gap characteristics of infinite periodic structures with single or bi-material cells of assumed initial periodic topology.

In this paper, no initial periodic topology is assumed and the optimization is carried out over the entire structure rather than on an individual cell. In this manner, actual boundary conditions can be imposed, the topology of finite structures can be directly optimized, and the obtained performance predictions can be realistic. Accordingly, the topology optimization approach adopted here considers the design space to be only the unit cell of the periodic plate and replicates the topology of the unit cell over the entire structure by enforcing a periodicity constraint. Then, the topology, i.e. thickness distribution over the unit cell is selected to maximize the fundamental frequency of the entire plate. In this way, the topology optimization process is carried out very fast as it is limited to selecting the thickness distribution of a LOCAL unit cell while the design objective describes the GLOBAL performance of a periodic assembly of the local unit cell.

This paper is organized in four sections and one appendix. In Section 1, a brief introduction is presented. In Section 2, a finite element model is presented to describe the vibration of Mindlin

* Corresponding author. Tel.: +1 301 405 5216; fax: +1 301 405 8331.
E-mail address: baz@eng.umd.edu (A. Baz).

0168-874X/$ - see front matter © 2008 Elsevier B.V. All rights reserved.
doi:10.1016/j.finel.2008.01.016

Author's personal copy

Nomenclature

A^e	element surface area	T^e	element kinetic energy
$\mathbf{B}$	matrix of differential operators in strain–displacement relationship	$\mathbf{u}$	displacement vector
		U^e	element potential energy
$\mathbf{D}$	constitutive matrix	u, v, w	displacement components
E	elasticity modulus	V^e	element volume
$\mathbf{F}$	force vector	vf	volume fraction
f	natural frequency (Hz)	x, y, z	physical coordinates
$\mathbf{h}$	vector of the thickness of elements	β	lower bound on natural frequencies
$h^e, h_{\min}, h_{\max}$	element current, minimum and maximum thicknesses	$\boldsymbol{\delta}$	vector of degrees of freedom
		ϕ_x, ϕ_y	angular rotations
$\mathbf{k}$	wave vector	$\boldsymbol{\varepsilon}$	strain vector
$\mathbf{K}^e, \mathbf{K}_c, \mathbf{K}$	element, cell, and global stiffness matrices	$\boldsymbol{\sigma}$	stress vector
		$\rho, \boldsymbol{\rho}$	material density and density matrix
$\mathbf{M}^e, \mathbf{M}_c, \mathbf{M}$	element, cell, and global mass matrices	υ	Poisson's ratio
N_{el}, N_{cel}, N_m	number of elements, cells, and modes	ω	natural frequency (rad/s)
$\mathbf{N}$	matrix of interpolation functions		

plates. Section 3 presents several numerical examples and Section 4 summarizes the conclusions of this study. Derivation of the basic finite element matrices is given in the appendix.

2. Mathematical model

In this section, a finite element model is presented to describe the vibration of Mindlin plates based on the approach outlined by Reddy [12]. The model is then integrated with an optimization algorithm that enforces periodicity in order to determine the optimal topologies of plates with various periodic configurations.

2.1. Finite element modeling

Consider any point at a distance z from the neutral plane of the plate shown in Fig. 1 undergoing lateral motion. The displacement has three components $\{u, v, w\}$ in the x, y, and z directions, respectively. The first two components are given by

$$u = z\phi_x, \quad v = z\phi_y, \tag{1}$$

where ϕ_x and ϕ_y are, respectively, the angular rotations of the mid-plane about the x- and y-axes. The plate is divided into four-node finite elements of thickness h^e, where the superscript e designates the element number. Each node has three degrees of freedom, w, ϕ_x, and ϕ_y making a total of 12 degrees of freedom per element. Within this element, the displacement vector $\mathbf{u}^e = \{w, \phi_x, \phi_y\}^T$ is approximated by

$$\mathbf{u}^e = \mathbf{N} \cdot \boldsymbol{\delta}^e, \tag{2}$$

where $\mathbf{N}$ is a 3×12 matrix including the bilinear Lagrange interpolation functions while $\boldsymbol{\delta}^e$ is a 12×1 vector with all 12 degrees of freedom of this element. The strain–displacement relationship for a plate element under bending is given by

$$\boldsymbol{\varepsilon} = \begin{Bmatrix} z\dfrac{\partial \phi_x}{\partial x} \\ z\dfrac{\partial \phi_x}{\partial x} \\ \phi_y + \dfrac{\partial w}{\partial y} \\ \phi_x + \dfrac{\partial w}{\partial x} \\ z\left(\dfrac{\partial \phi_x}{\partial y} + \dfrac{\partial \phi_y}{\partial x}\right) \end{Bmatrix} = \mathbf{B} \cdot \mathbf{u}^e, \tag{3}$$

where $\mathbf{B}$ is a matrix of differential operators

$$\mathbf{B} = \begin{bmatrix} 0 & z\dfrac{\partial}{\partial x} & 0 \\ 0 & 0 & z\dfrac{\partial}{\partial y} \\ \dfrac{\partial}{\partial y} & 0 & 1 \\ \dfrac{\partial}{\partial x} & 1 & 0 \\ 0 & z\dfrac{\partial}{\partial y} & z\dfrac{\partial}{\partial x} \end{bmatrix}. \tag{4}$$

The approximation in Eq. (2) together with Eq. (3) is used to express the strain in terms of the element degrees of freedom δ^e as follows:

$$\boldsymbol{\varepsilon} = \mathbf{B} \cdot \mathbf{N} \cdot \boldsymbol{\delta}^e. \tag{5}$$

Therefore, the variation in the potential energy in the element δU^e due to a virtual change in the strain $\delta\boldsymbol{\varepsilon}$ is

$$\delta U^e = \int_V \delta\boldsymbol{\varepsilon}^T \cdot \boldsymbol{\sigma}\, dV, \tag{6}$$

Author's personal copy

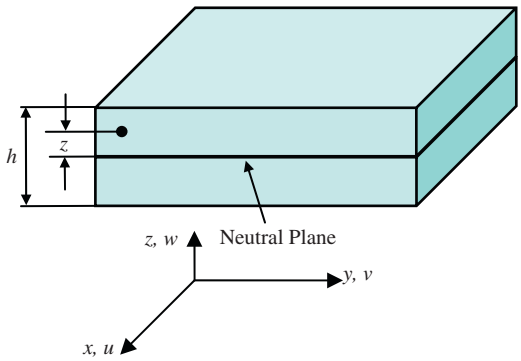

Fig. 1. Schematic of a plate element.

where V denotes the volume. Eq. (6) can be expressed in terms of strain only using the constitutive relation for small elastic strains $\boldsymbol{\sigma} = \mathbf{D} \cdot \boldsymbol{\varepsilon}$

$$\delta U^e = \int_V \delta \boldsymbol{\varepsilon}^{\mathrm{T}} \cdot \mathbf{D} \cdot \boldsymbol{\varepsilon} \, \mathrm{d}V, \tag{7}$$

where $\mathbf{D}$ is the constitutive matrix. Therefore, the variation in the element potential energy δU^e due to a virtual displacement $\delta \boldsymbol{\delta}^e$ is

$$\delta U^e = \delta \boldsymbol{\delta}^{e^{\mathrm{T}}} \cdot \mathbf{K}^e \cdot \boldsymbol{\delta}^e, \tag{8}$$

where $\mathbf{K}^e$ the element stiffness matrix is defined as

$$\mathbf{K}^e = \int_{A^e} \int_{-h/2}^{h/2} \mathbf{N}^{\mathrm{T}} \cdot \mathbf{B}^{\mathrm{T}} \cdot \mathbf{D} \cdot \mathbf{B} \cdot \mathbf{N} \, \mathrm{d}z \, \mathrm{d}A^e, \tag{9}$$

where A^e denotes the area. From the expression of the strain vector in Eq. (3), it can be easily noticed that $\mathbf{K}^e$ will incorporate terms in h^e and h^{e^3} as outlined in the appendix, such that

$$\mathbf{K}^e = h^e \mathbf{K}_1^e + h^{e^3} \mathbf{K}_3^e, \tag{10}$$

where the matrices $\mathbf{K}_1^e$ and $\mathbf{K}_3^e$ are given in the appendix.

In a similar fashion, the variation in the element kinetic energy δT^e due to a virtual displacement $\delta \mathbf{u}^e$ can be determined from:

$$\delta T^e = \int_V \delta \dot{\mathbf{u}}^{\mathrm{T}} \cdot \boldsymbol{\rho} \cdot \dot{\mathbf{u}} \, \mathrm{d}V, \tag{11}$$

where $\boldsymbol{\rho}$ is defined as

$$\boldsymbol{\rho} = \rho \begin{bmatrix} 1 & 0 & 0 \\ 0 & z^2 & 0 \\ 0 & 0 & z^2 \end{bmatrix}, \tag{12}$$

where ρ is the density of the plate material. In Eq. (11), $\mathbf{u}$ can be substituted by the approximation given in Eq. (2) to yield

$$\delta T^e = \delta \dot{\boldsymbol{\delta}}^{e^{\mathrm{T}}} \cdot \mathbf{M}^e \cdot \dot{\boldsymbol{\delta}}^e, \tag{13}$$

where $\mathbf{M}^e$ is the element mass matrix defined as

$$\mathbf{M}^e = \int_{A^e} \int_{-h/2}^{h/2} \mathbf{N}^{\mathrm{T}} \cdot \boldsymbol{\rho} \cdot \mathbf{N} \, \mathrm{d}z \, \mathrm{d}A^e. \tag{14}$$

Again, it is clear that $\mathbf{M}^e$ will incorporate terms in h^e and h^{e^3} as indicated in the appendix such that

$$\mathbf{M}^e = h^e \mathbf{M}_1^e + h^{e^3} \mathbf{M}_3^e, \tag{15}$$

where $\mathbf{M}_1^e$ and $\mathbf{M}_3^e$ are described in the appendix.

For a harmonic motion with angular frequency ω,

$$\dot{\boldsymbol{\delta}} = \mathrm{i}\omega \boldsymbol{\delta}, \tag{16}$$

where $\mathrm{i} = \sqrt{-1}$. Therefore, the expression for δT^e becomes

$$\delta T^e = -\omega^2 \delta \boldsymbol{\delta}^{e^{\mathrm{T}}} \cdot \mathbf{M}^e \cdot \boldsymbol{\delta}^e. \tag{17}$$

Applying the principal of virtual work yields

$$\sum_{i=1}^{N_{\mathrm{el}}} (\delta U^e + \delta T^e) = 0, \tag{18}$$

where N_{el} is the total number of elements. Using the element energies in Eqs. (8) and (17) the resulting equation of motion is

$$(\mathbf{K} - \omega^2 \mathbf{M}) \boldsymbol{\delta} = \mathbf{0}, \tag{19}$$

where $\boldsymbol{\delta}$ is the global vector of degrees of freedom of all elements, while $\mathbf{K}$ and $\mathbf{M}$ are the global stiffness and mass matrices calculated using the expressions of the element stiffness and mass matrices in Eqs. (9) and (14) as follows:

$$\mathbf{K} = \sum_{e=1}^{N_{\mathrm{el}}} \mathbf{K}^e, \quad \mathbf{M} = \sum_{e=1}^{N_{\mathrm{el}}} \mathbf{M}^e. \tag{20}$$

Eq. (19) represents the governing equation of a plate undergoing free lateral oscillations at a frequency $\omega = 2\pi f$. The essential boundary conditions are imposed by setting the constrained degrees of freedom in the vector $\boldsymbol{\delta}$ to prescribed values. The natural frequencies f_{n} and the corresponding mode shapes are determined by solving the eigenvalue problem of Eq. (19).

2.2. Topology optimization

The finite element model developed in the previous section is integrated with an optimization algorithm in order to generate the optimal topologies of plates with various periodic configurations. The objective is to maximize the fundamental frequency f_1 of the plate while maintaining periodicity of the plate. Periodicity is applied by dividing the plate into N_{c} identical cells. The unit cell is repeated N_x times along the x-axis and N_y times along the y-axis such that $N_{\mathrm{c}} = N_x \ N_y$. Each of these cells has N_{elc} elements with thicknesses $\mathbf{h}_i = \{h^1 \ h^2 \ \ldots \ h^{N_{\mathrm{elc}}}\}$ where $i = 1, \ldots, N_{\mathrm{c}}$. Note that $N_{\mathrm{elc}} = N_{\mathrm{c}x} N_{\mathrm{c}y}$ where $N_{\mathrm{c}x}$ and $N_{\mathrm{c}y}$ denote the number of elements along the x- and y-axes in each cell as shown in Fig. 2.

Accordingly, the topology optimization approach adopted here considers the design space to be only the unit cell of the periodic plate and replicates the topology of the unit cell over the entire structure by enforcing a periodicity constraint. Then,

Author's personal copy

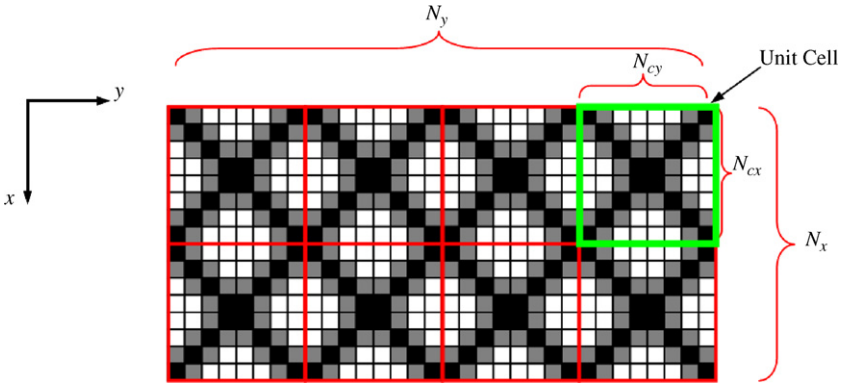

Fig. 2. Schematic of a plate element.

the topology, i.e. thickness distribution over the unit cell is selected to maximize the fundamental frequency of the entire plate. In this way, the topology optimization process is carried out very fast as it is limited to selecting the thickness distribution of a LOCAL unit cell while the design objective describes the GLOBAL performance of a periodic assembly of the local unit cell.

The bound formulation described in Bendsøe and Sigmund [13] is used to optimize the plate topology while enforcing periodicity as follows:

$$\left\langle \begin{array}{lll} \max\limits_{\mathbf{h}} \beta, & & \\ \text{such that} & & \\ \omega_i > \beta, & & i = N_{\mathrm{m}}, \\ \mathbf{h}_1 = \mathbf{h}_2 = \cdots = \mathbf{h}_{N_{\mathrm{c}}}, & & \\ (\mathbf{K} - \omega_i^2 \mathbf{M})\boldsymbol{\delta}_i = \mathbf{0}, & & i = N_{\mathrm{m}}, \\ \sum\limits_{e=1}^{N_{\mathrm{elc}}} h^e A^e \leqslant vf \times h_{\max} \sum\limits_{e=1}^{N_{\mathrm{elc}}} A^e, & & \\ 0 < h_{\min} \leqslant h^e \leqslant h_{\max}, & & e = 1, 2, \cdots, N_{\mathrm{elc}} \end{array} \right\rangle, \tag{21}$$

where β is a lower bound of the natural frequencies, N_{m} is the number of the considered lowest natural frequencies, $h_{\min}$ and $h_{\max}$ are the minimum and maximum bounds on the plate thickness, respectively. The optimization formulation shown in Eq. (21) simply maximizes the lower bound on the natural frequencies of the whole plate by controlling only the thicknesses of one cell while the objective function accounts for the contributions of all cells. Note that the periodicity is imposed by constraining the thicknesses of each cell to be equal as defined by the equality constraint that appears in the fourth line of Eq. (21).

An important part of the optimization process is the sensitivity analysis in which the effect of the design variables $\mathbf{h}$ on the optimization function β is considered. The governing equation (19) is made scalar by premultiplying it by $\boldsymbol{\delta}_i^{\mathrm{T}}$ and differentiating it with respect to each component of $\mathbf{h}$ to give

$$\boldsymbol{\delta}_i^{\mathrm{T}} \cdot \left(\frac{\partial \mathbf{K}}{\partial h^e} - \frac{\partial \omega_i^2}{\partial h^e}\mathbf{M} - \omega_i^2 \frac{\partial \mathbf{M}}{\partial h^e} \right) \cdot \boldsymbol{\delta}_i = \mathbf{0} \tag{22}$$

from which the sensitivities can be extracted as

$$\frac{\partial \omega_i^2}{\partial h^e} = \boldsymbol{\delta}_i^{\mathrm{T}} \cdot \left(\frac{\partial \mathbf{K}}{\partial h^e} - \omega_i^2 \frac{\partial \mathbf{M}}{\partial h^e} \right) \cdot \boldsymbol{\delta}_i, \tag{23}$$

where the mode shapes $\boldsymbol{\delta}_i$ have been normalized with respect to the mass matrix $\mathbf{M}$. The effect of periodicity is manifested in the derivatives of the global mass and stiffness matrices with respect to $\mathbf{h}$ as

$$\frac{\partial \mathbf{K}}{\partial h^e} = \sum_{j=1}^{N_{\mathrm{c}}} \mathbf{K}_1^{e(j)} + 3h^{e^2} \mathbf{K}_3^{e(j)} \quad \text{and}$$

$$\frac{\partial \mathbf{M}}{\partial h^e} = \sum_{j=1}^{N_{\mathrm{c}}} \mathbf{M}_1^{e(j)} + 3h^{e^2} \mathbf{M}_3^{e(j)}, \tag{24}$$

where Eqs. (10) and (15) have been used and $e(j)$ denotes the eth element of the jth cell.

In many applications, it is desirable to have the optimized topology in a 0–1 state by penalizing intermediate values. A very popular technique is the '*solid isotropic material with penalization*' (SIMP) discussed in Bendsøe and Sigmund [13]. Although mandatory in some cases, penalization has some drawbacks as it leads to less optimal solutions, and may also yield entirely different topologies depending on the selection of the penalty factor. In this paper, no penalization is applied and the optimization algorithm is free to choose any intermediate values of h^e.

2.3. Frequency bands

In this section, the theory behind the computation of the frequency bands is presented in order to investigate the stop bands created by the plate periodic patterns. Fig. 3 shows a square cell extending along the domain of the wave vector $\mathbf{k} = \{k_1 \;\; k_2\} = [-\pi \;\; \pi]^2$.

The cell is governed by the following equation of motion:

$$(\mathbf{K}_{\mathrm{c}} - \omega^2 \mathbf{M}_{\mathrm{c}})\boldsymbol{\delta}_{\mathrm{c}} = \mathbf{0}, \tag{25}$$

where $\mathbf{K}_{\mathrm{c}}$, $\mathbf{M}_{\mathrm{c}}$, and $\boldsymbol{\delta}_{\mathrm{c}}$ are the stiffness matrix, mass matrix, and the degrees of freedom vector of all nodes in the cell.

Author's personal copy

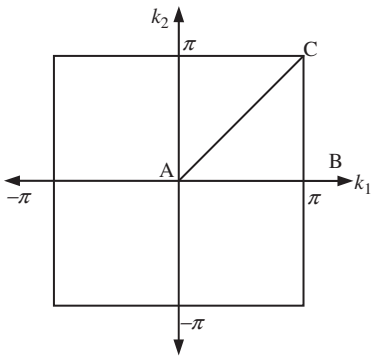

Fig. 3. Boundaries of Brillouin Zone.

The degrees of freedom can be divided into five groups; $\boldsymbol{\delta}_i$, $\boldsymbol{\delta}_1$, $\boldsymbol{\delta}_2$, $\boldsymbol{\delta}_3$, and $\boldsymbol{\delta}_4$ which belong to the interior, left, bottom, right, and top nodes, respectively. Therefore, Eq. (25) can be written as

$$\begin{bmatrix} \mathbf{K}_{ii} & \mathbf{K}_{i1} & \mathbf{K}_{i2} & \mathbf{K}_{i3} & \mathbf{K}_{i4} \\ \mathbf{K}_{1i} & \mathbf{K}_{11} & \mathbf{K}_{12} & \mathbf{K}_{13} & \mathbf{K}_{14} \\ \mathbf{K}_{2i} & \mathbf{K}_{21} & \mathbf{K}_{22} & \mathbf{K}_{23} & \mathbf{K}_{24} \\ \mathbf{K}_{3i} & \mathbf{K}_{31} & \mathbf{K}_{32} & \mathbf{K}_{33} & \mathbf{K}_{34} \\ \mathbf{K}_{4i} & \mathbf{K}_{41} & \mathbf{K}_{42} & \mathbf{K}_{43} & \mathbf{K}_{44} \end{bmatrix} \begin{Bmatrix} \boldsymbol{\delta}_i \\ \boldsymbol{\delta}_1 \\ \boldsymbol{\delta}_2 \\ \boldsymbol{\delta}_3 \\ \boldsymbol{\delta}_4 \end{Bmatrix} = \begin{Bmatrix} 0 \\ \mathbf{F}_1 \\ \mathbf{F}_2 \\ \mathbf{F}_3 \\ \mathbf{F}_4 \end{Bmatrix}, \tag{26}$$

where $\mathbf{K}_{jk}$ are the appropriate sub-matrices of the dynamic stiffness matrix.

Periodicity implies that $\boldsymbol{\delta}_3 = e^{ik_1}\boldsymbol{\delta}_1$, $\boldsymbol{\delta}_4 = e^{ik_2}\boldsymbol{\delta}_2$, $\mathbf{F}_3 = -e^{ik_1}\mathbf{F}_1$, and $\mathbf{F}_4 = -e^{ik_2}\mathbf{F}_2$. Hence, Eq. (26) becomes

$$\begin{bmatrix} \mathbf{K}_{ii} & \mathbf{K}_{i1} + e^{ik_1}\mathbf{K}_{i3} & \mathbf{K}_{i2} + e^{ik_2}\mathbf{K}_{i4} \\ \mathbf{K}_{1i} & \mathbf{K}_{11} + e^{ik_1}\mathbf{K}_{13} & \mathbf{K}_{12} + e^{ik_2}\mathbf{K}_{14} \\ \mathbf{K}_{2i} & \mathbf{K}_{21} + e^{ik_1}\mathbf{K}_{23} & \mathbf{K}_{22} + e^{ik_2}\mathbf{K}_{24} \\ \mathbf{K}_{3i} & \mathbf{K}_{31} + e^{ik_1}\mathbf{K}_{33} & \mathbf{K}_{32} + e^{ik_2}\mathbf{K}_{34} \\ \mathbf{K}_{4i} & \mathbf{K}_{41} + e^{ik_1}\mathbf{K}_{43} & \mathbf{K}_{42} + e^{ik_2}\mathbf{K}_{44} \end{bmatrix} \begin{Bmatrix} \boldsymbol{\delta}_i \\ \boldsymbol{\delta}_1 \\ \boldsymbol{\delta}_2 \end{Bmatrix} = \begin{Bmatrix} 0 \\ \mathbf{F}_1 \\ \mathbf{F}_2 \\ -e^{ik_1}\mathbf{F}_1 \\ -e^{ik_2}\mathbf{F}_2 \end{Bmatrix}. \tag{27}$$

Multiplying the fourth and fifth rows of Eq. (27) by e^{-ik_1} and e^{-ik_2}, and adding them to the second and third rows, respectively nullifies the force vector and results in the following eigenvalue problem [8]:

$$(\mathbf{K}_c(\mathbf{k}) - \omega^2(\mathbf{k})\mathbf{M}_c)\boldsymbol{\delta}_c = \mathbf{0}, \tag{28}$$

in which the mass matrix is independent of the wave vector. One can easily show that $\mathbf{K}_c(\mathbf{k})$ has complex components but still symmetric and yields real $\omega(\mathbf{k})$. Plotting of the frequency bands as a function of $\mathbf{k}$ can be significantly simplified by searching along the boundaries of the irreducible Brillouin zone defined by the polygon ABC shown in Fig. 3.

3. Numerical examples

The model developed in the previous section is applied to some test cases. The adopted optimization procedure is summarized in Fig. 4. The procedure relies on using the Method of Moving Asymptotes (MMA) proposed by Svanberg [14] to select the cell optimal thickness distribution. It is worth mentioning that the computation time is mainly determined by building/solving the finite element model and using the MMA. These two steps are represented by the second and third blocks in Fig. 4. The former mainly depends on the total number of elements N_{el}, while the latter mainly depends on the number of design variables N_{elc}. Applying periodicity limits N_{elc}, significantly decreases the processing time per iteration as well as the number of iterations needed for convergence.

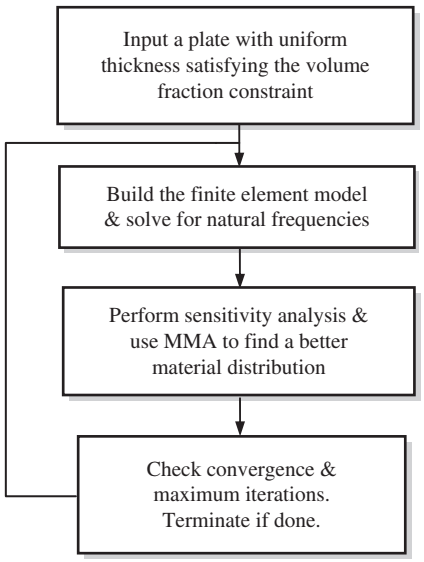

Fig. 4. Block diagram for the optimization procedure.

3.1. Plates with simply supported-free–simply supported-free boundaries

In this section, rectangular plates with sides 300 and 150 mm are considered. The plates are made of aluminum with $h_{min} = 0.5$ mm and $h_{max} = 5$ mm and are divided into 32×16 square elements. The boundary conditions are chosen such that the plate is simply supported on the long edges and free on the short ones. The maximum number of iterations is set to 200. Four cases are considered; non-periodic in which the plate is optimized without enforcing any periodicity, 2×1 periodic in which the plate is divided into two square cells, 4×2 periodic in which the plate is divided into eight square cells, and 8×4 periodic in which the plate is divided into 30 two rectangular cells. In all the four cases, modal analysis is carried out for the final topology and the lowest 50 modes are extracted which are used with a standard modal reduction technique to predict the displacement amplitude at the midpoint of the right edge as a result of a harmonic force of unit amplitude at the midpoint of the left edge.

Fig. 5 shows some of the intermediate and final iterations of the non-periodic case. It is clear that the optimum non-periodic topology is symmetric rather than periodic.

Author's personal copy

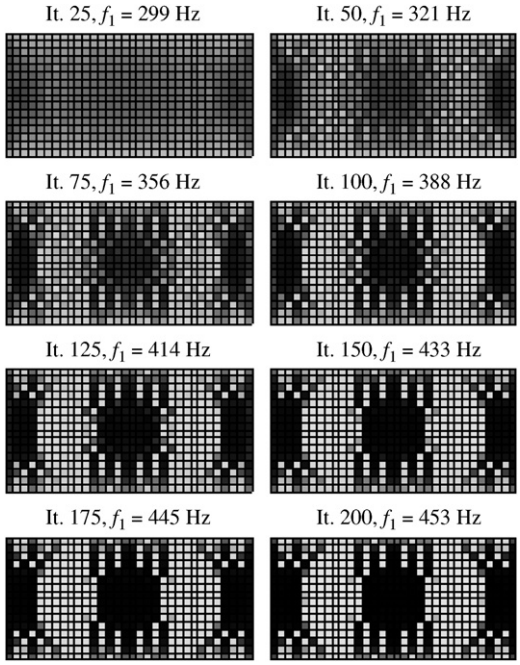

Fig. 5. Densities of a non-periodic plate at iteration numbers 25, 50, . . . , 200, $vf = 0.5$, $h_{min} = 0.5$ mm, $h_{max} = 5$ mm.

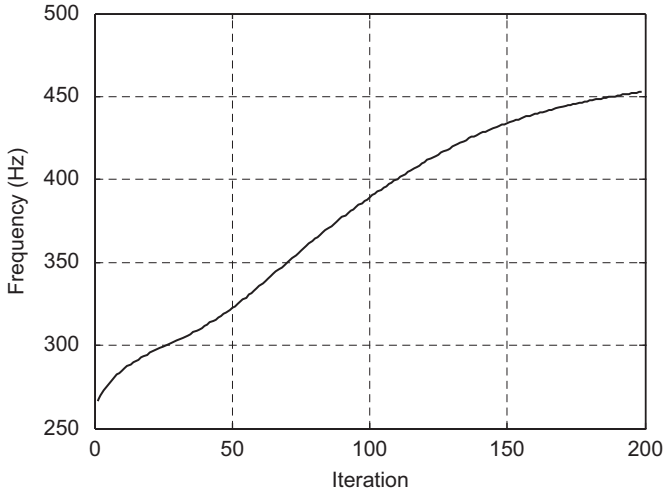

Fig. 6. Development of the fundamental frequency f_1 of a non-periodic plate $vf = 0.5$, $h_{min} = 0.5$ mm, $h_{max} = 5$ mm.

Fig. 6 shows the evolution of the fundamental frequency along the optimization process where f_1 has evolved to 170% of the plain case in 200 iterations.

Fig. 7 shows the frequency response at the midpoint of the left edge in a logarithmic scale of the optimal topology as compared to the frequency response of a plain plate. It is obvious that the symmetry has created some narrow stop bands below 500 Hz and around 1800 Hz.

Fig. 8 shows some of the intermediate and final iterations of the 2 × 1 periodic case.

Fig. 9 shows the evolution of the fundamental frequency along the optimization process where f_1 has evolved to 171%

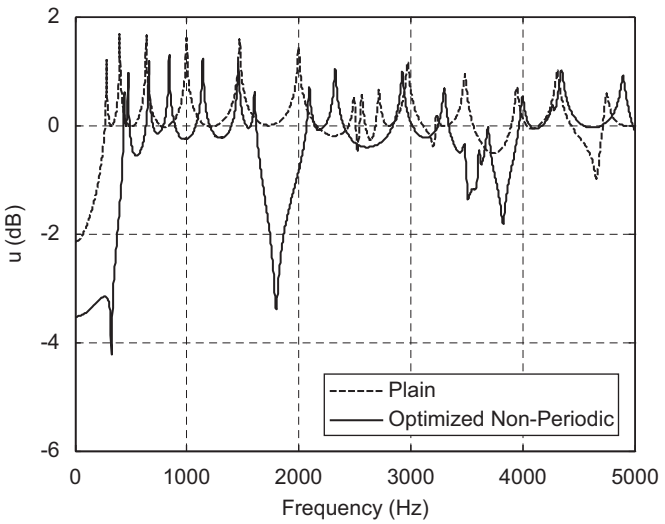

Fig. 7. Frequency response of a non-periodic plate at the center of the right edge excited with a harmonic force at the center of the left edge $vf = 0.5$, $h_{min} = 0.5$ mm, $h_{max} = 5$ mm.

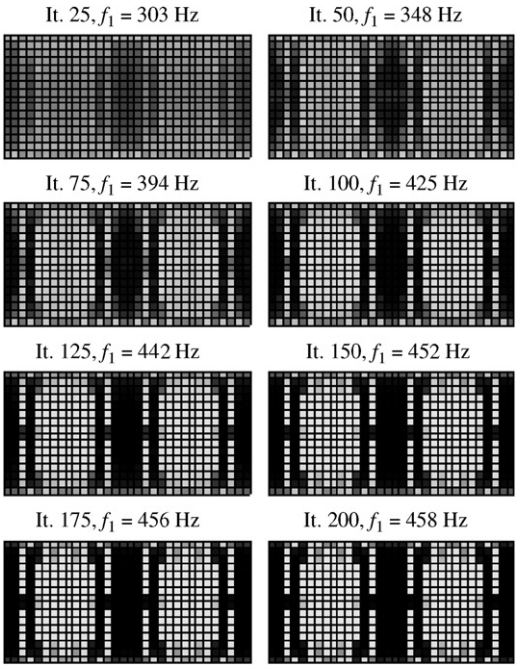

Fig. 8. Densities of a 2 × 1 periodic plate at iteration numbers 25, 50, . . . , 200, $vf = 0.5$, $h_{min} = 0.5$ mm, $h_{max} = 5$ mm.

of the plain case in 200 iterations. This is little bit higher than the non-periodic case. This is attributed to dealing with half the number of the design variables, which makes the optimization converge faster than the other case.

Fig. 10 shows the frequency response at the midpoint of the left edge in a logarithmic scale of the optimal topology as compared to the frequency response of a plain plate. One can easily notice that the optimal 2 × 1 periodic plate is as good as the non-periodic plate in terms of the fundamental frequency but we do not gain much in terms of the stop bands.

Author's personal copy

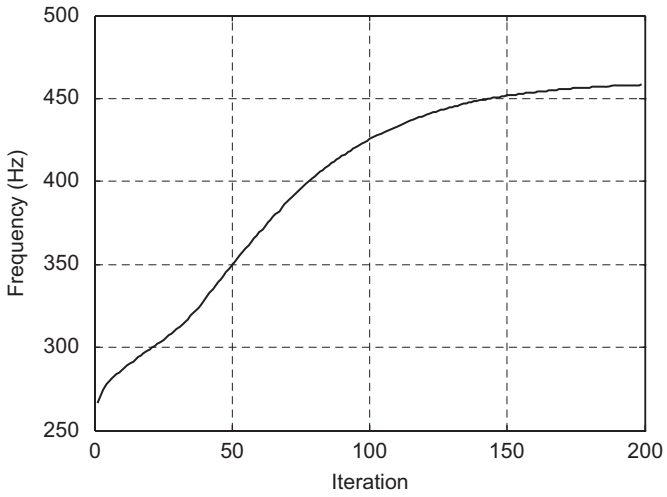

Fig. 9. Development of the fundamental frequency f_1 of a 2×1 periodic plate, $vf = 0.5$, $h_{min} = 0.5$ mm, $h_{max} = 5$ mm.

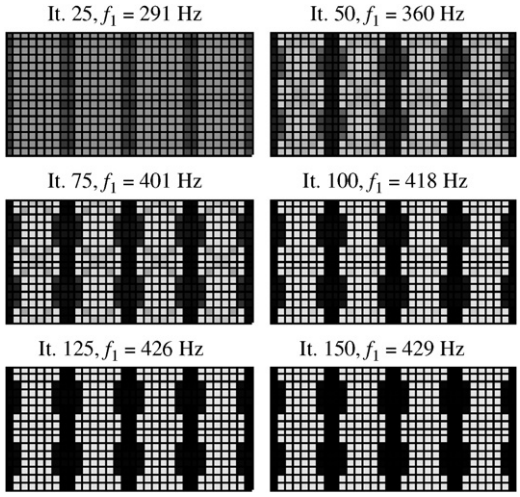

Fig. 11. Densities of a 4×2 periodic plate at iteration numbers 25, 50, . . . , 200, $vf = 0.5$, $h_{min} = 0.5$ mm, $h_{max} = 5$ mm.

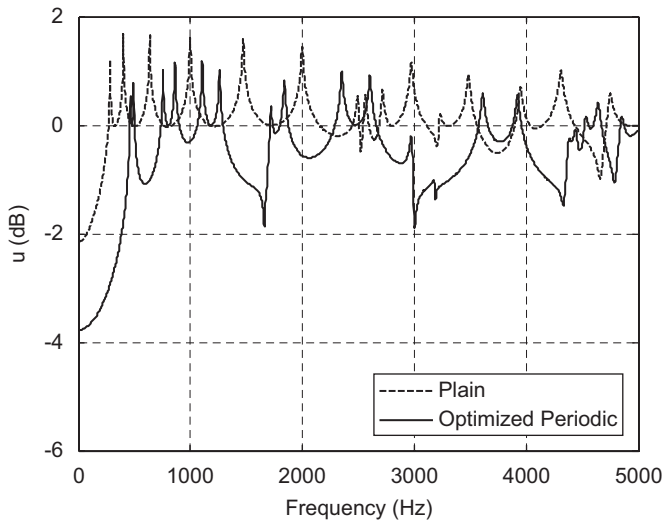

Fig. 10. Frequency response of a 2×1 periodic plate at the center of the right edge excited with a harmonic force at the center of the left edge, $vf = 0.5$, $h_{min} = 0.5$ mm, $h_{max} = 5$ mm.

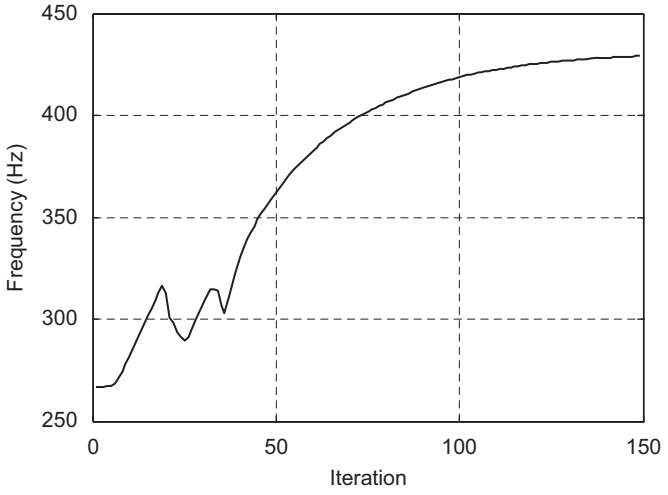

Fig. 12. Development of the fundamental frequency f_1 of a 4×2 periodic plate, $vf = 0.5$, $h_{min} = 0.5$ mm, $h_{max} = 5$ mm.

Fig. 11 shows some of the intermediate and final iterations of a 4×2 periodic plate.

Fig. 12 shows the evolution of the fundamental frequency along the optimization process where f_1 has evolved to 163% of the plain case. That is to say similar to the non-periodic optimization. It is clear that convergence is much faster than previous cases. It is worth mentioning that in this case N_m is chosen as 3 since using less modes resulted in jumps during the evolution of f_1.

Fig. 13 shows the frequency response at the midpoint of the left edge in a logarithmic scale of the optimal topology as compared to the frequency response of a plain plate. Much wider stop bands are attained in this configuration.

Figs. 14–16 show the corresponding characteristics for an 8×4 periodic plate.

The frequency bands of the 2×1 as compared to the 4×2 and 8×4 periodic plates according to the discussion in Section 2.3 are plotted in Fig. 17. The figure displays the effect of the propagation direction, as outlined in Fig. 3, on the stop band characteristics of the plates. Note that this plot is in effect a plot of the dispersion characteristics of these plates [8]. The figure shows that indeed periodicity develops several stop bands over the spectrum. The periodicity pattern can be chosen to suppress vibration in desired frequency ranges and propagation direction.

3.2. Plates with fixed boundaries

In this section, square plates with sides 300 and 300 mm are considered. The plates are made of aluminum with $h_{min} = 0.5$ mm and $h_{max} = 5$ mm and are divided into 16×16 square elements. The boundary conditions are chosen such that the plate is fixed along all its edges. The maximum number of iterations

Author's personal copy

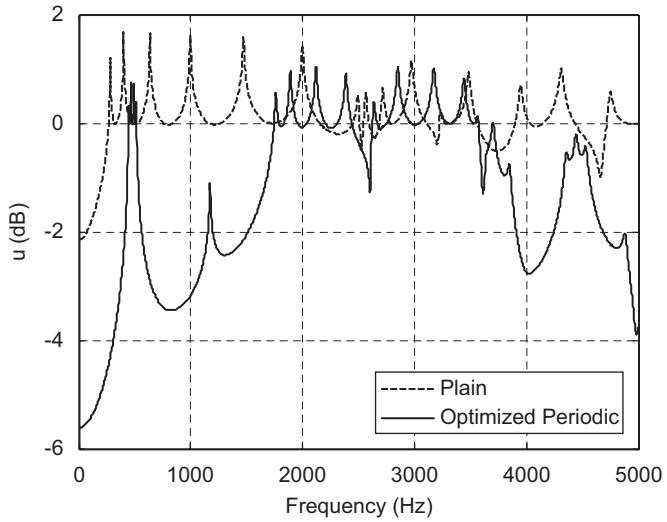

Fig. 13. Frequency response of a 4×2 plate at the center of the right edge when excited with a harmonic force at the center of the left edge, $vf = 0.5$, $h_{\min} = 0.5$ mm, $h_{\max} = 5$ mm.

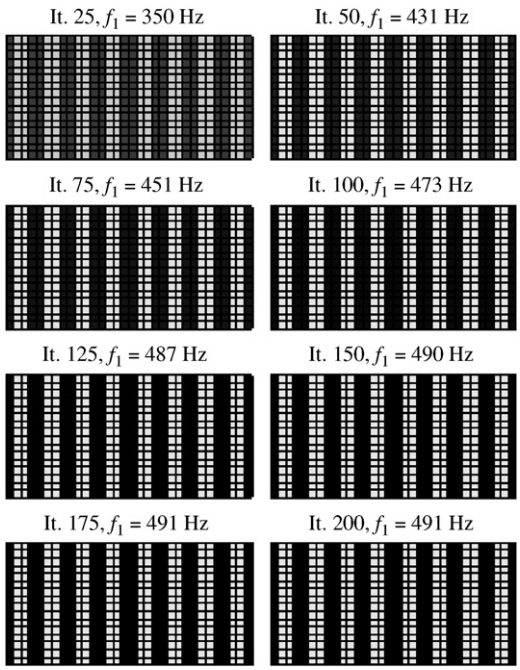

Fig. 14. Densities of an 8×4 periodic plate at iteration numbers 25, 50, . . . , 200, $vf = 0.5$, $h_{\min} = 0.5$ mm, $h_{\max} = 5$ mm.

is set to 200. Two cases are considered; non-periodic and 2×2 periodic in which the plate is divided into four square cells. Figs. 18 and 19 show the evolution of the topology and fundamental frequencies for the non-periodic case. Fig. 20 shows the frequency response at the center of one quarter due to a unit force applied at the center of the diagonally opposite quarter.

Figs. 21 and 22, respectively, show the evolution of topology and fundamental frequencies for the periodic 2×2. Fig. 23 shows the frequency response at the center of one quarter due to a unit force applied at the center of the diagonally opposite quarter.

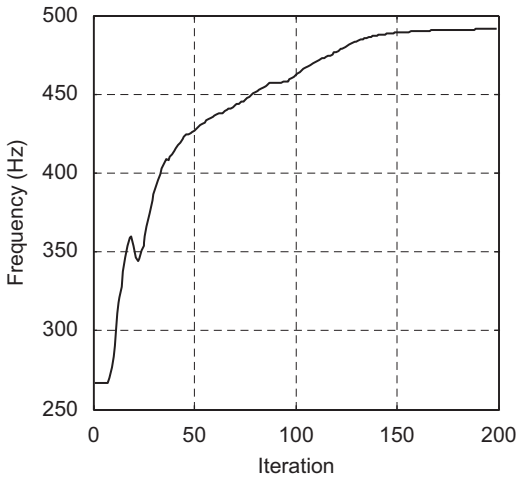

Fig. 15. Development of the fundamental frequency f_1 of an 8×4 periodic plate, $vf = 0.5$, $h_{\min} = 0.5$ mm, $h_{\max} = 5$ mm.

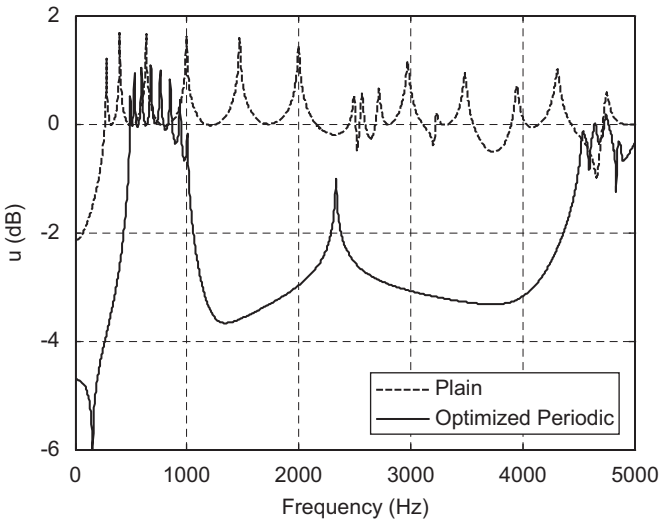

Fig. 16. Frequency response of an 8×4 periodic plate at the center of the right edge when excited with a harmonic force at the center of the left edge, $vf = 0.5$, $h_{\min} = 0.5$ mm, $h_{\max} = 5$ mm.

It is clear that although the natural frequency of the periodic design is smaller than that of the non-periodic, the stop bands are wider and extend over broad frequency bands as shown in the frequency band plot of Fig. 24.

4. Conclusions

In this paper, a finite element model is developed and used to evaluate the natural frequencies and predict the frequency response for Mindlin plates. The model is also used with a topology optimization algorithm to maximize the fundamental frequency while imposing periodicity on repeated cells of the plate. The proposed approach is applied to a fixed–free aluminum plates with a 2×1 aspect ratio and square plates with fixed–fixed boundaries.

Author's personal copy

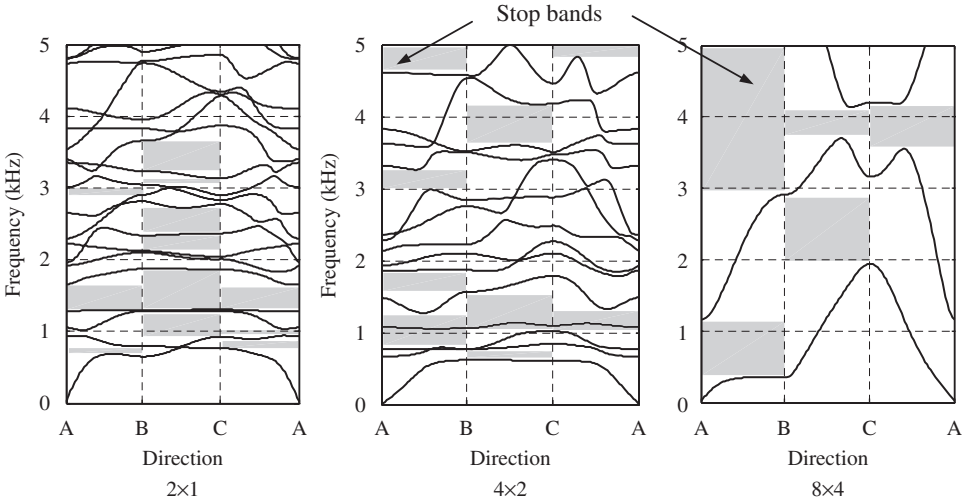

Fig. 17. Frequency bands of a 2×1, 4×2, and 8×4 periodic plates, $vf = 0.5$, $h_{\min} = 0.5\,\text{mm}$, $h_{\max} = 5\,\text{mm}$.

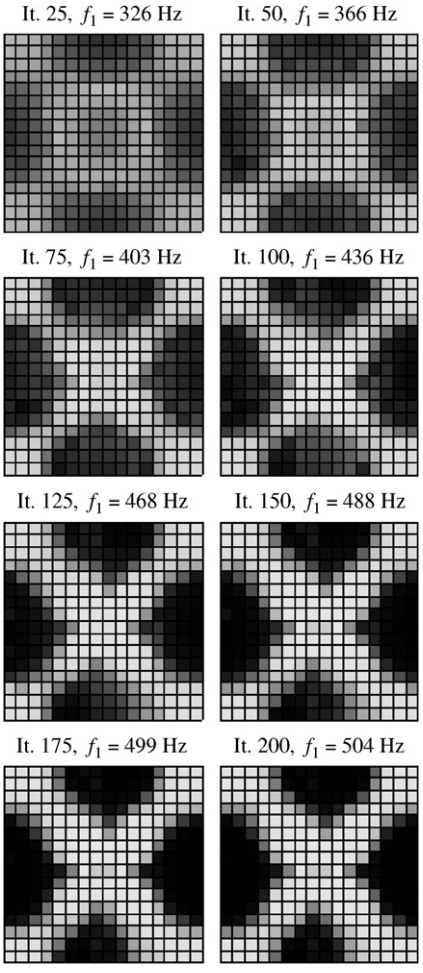

Fig. 18. Densities of a non-periodic square plate at iterations numbers 25, 50, ..., 200, $vf = 0.5$, $h_{\min} = 0.5\,\text{mm}$, $h_{\max} = 5\,\text{mm}$.

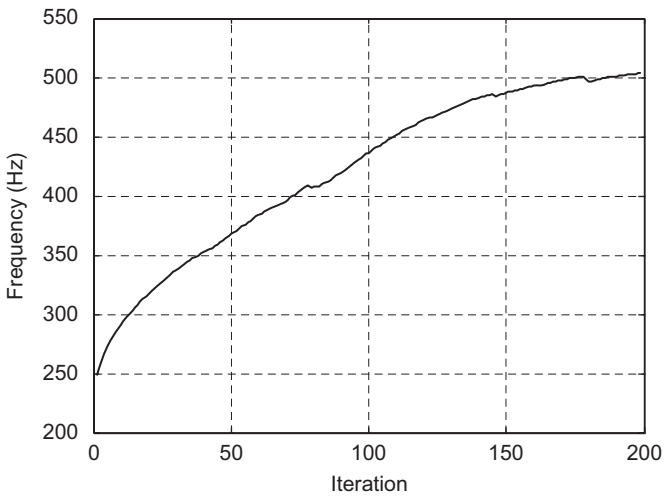

Fig. 19. Development of the fundamental frequency f_1 of a non-periodic square plate, $vf = 0.5$, $h_{\min} = 0.5\,\text{mm}$, $h_{\max} = 5\,\text{mm}$.

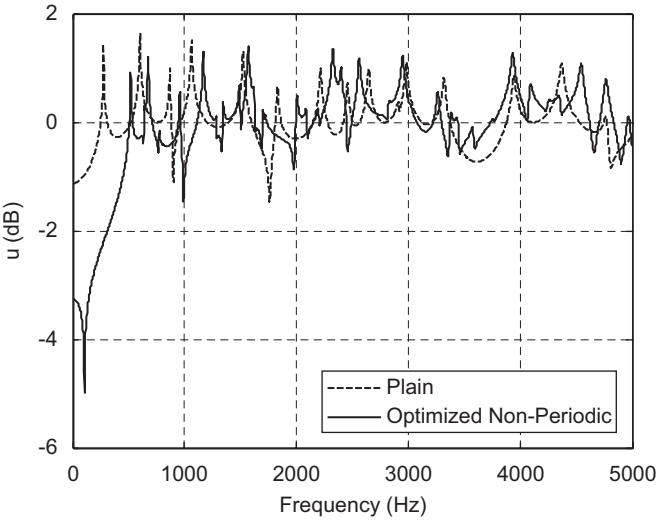

Fig. 20. Frequency response of a non-periodic square plate at the center of one quarter when excited with a harmonic force at the center of the diagonally opposite quarter, $vf = 0.5$, $h_{\min} = 0.5\,\text{mm}$, $h_{\max} = 5\,\text{mm}$.

It is important to note that proposed approach does not assume any initial periodic topology and the optimization is carried out over the entire structure rather than on an individual

Author's personal copy

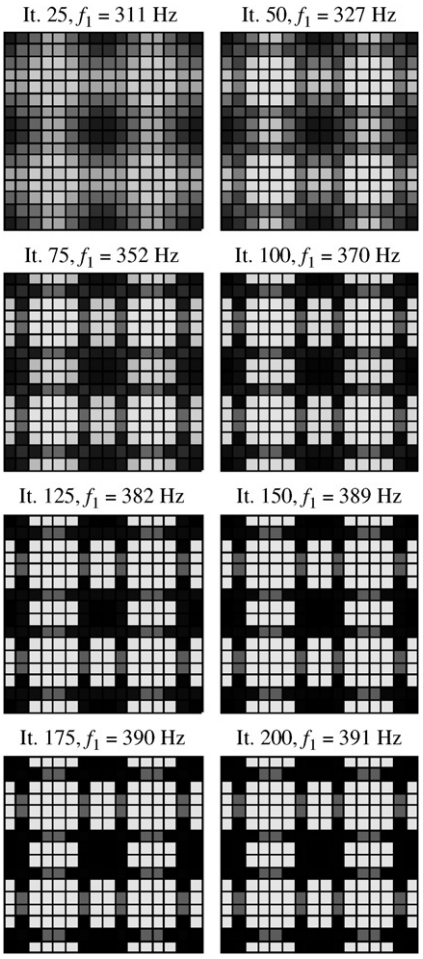

Fig. 21. Densities of a 2×2 periodic square plate at iterations numbers 25, 50, ..., 200, $vf = 0.5$, $h_{\min} = 0.5$ mm, $h_{\max} = 5$ mm.

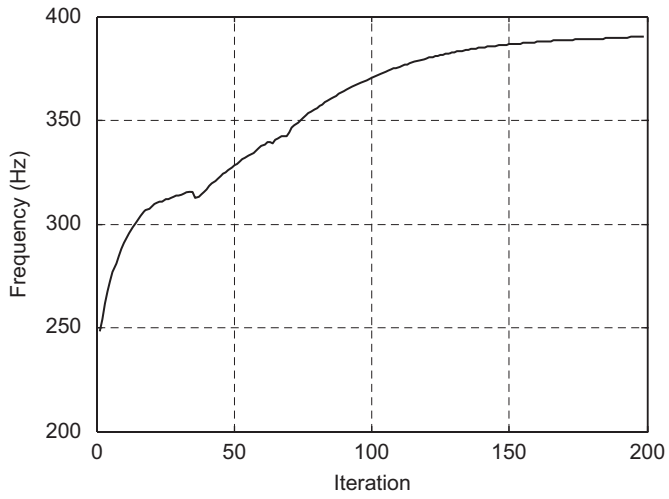

Fig. 22. Development of the fundamental frequency f_1 of a 2×2 periodic square plate, $vf = 0.5$, $h_{\min} = 0.5$ mm, $h_{\max} = 5$ mm.

cell. In this manner, actual boundary conditions can be imposed, the topology of finite structures can be directly optimized, and the obtained performance predictions can be

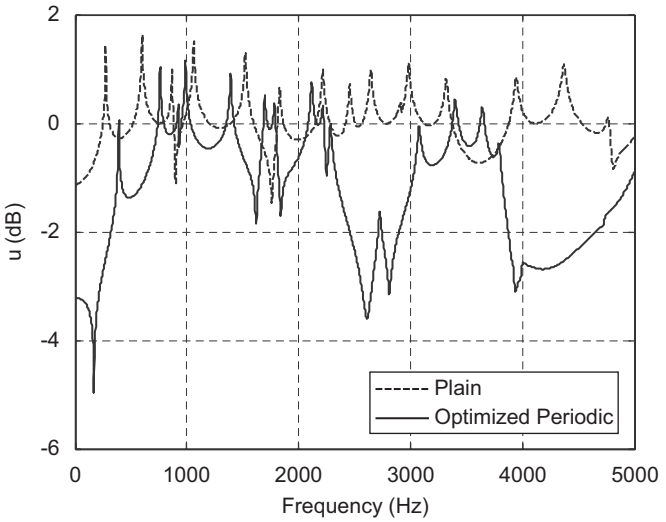

Fig. 23. Frequency response of a 2×2 periodic square plate at the center of one quarter when excited with a harmonic force at the center of the diagonally opposite quarter, $vf = 0.5$, $h_{\min} = 0.5$ mm, $h_{\max} = 5$ mm.

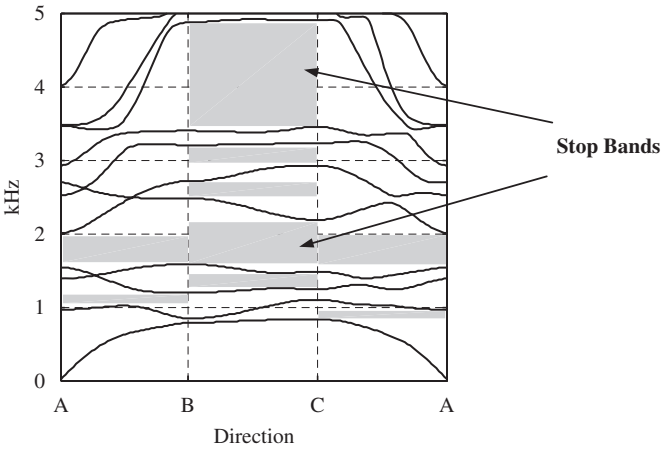

Fig. 24. Frequency bands of a 2×2 square periodic plates, $vf = 0.5$, $h_{\min} = 0.5$ mm, $h_{\max} = 5$ mm.

realistic. Accordingly, the topology optimization approach adopted here considers the design space to be only the unit cell of the periodic plate and replicates the topology of the unit cell over the entire structure by enforcing a periodicity constraint. Then, the topology, i.e. thickness distribution over the unit cell is selected to maximize the fundamental frequency of the entire plate. In this way, the topology optimization process is carried out in a computationally efficient manner as it is limited to selecting the thickness distribution of a LOCAL unit cell while the design objective describes the GLOBAL performance of a periodic assembly of the local unit cell.

The presented approach can be an invaluable design tool for many structures in order to control the wave propagation in an attempt to stop/confine the propagation of undesirable disturbances.

Author's personal copy

Acknowledgments

This work is funded by the Office of Naval Research (Grant number N000140610074). Special thanks are due to Dr. Kam Ng, the technical monitor, for his invaluable inputs and to Prof. K. Svanberg of the Royal Institute of Technology in Stockholm for supplying the Method of Moving Asymptotes code.

Appendix

For a square element of width a with $\boldsymbol{\delta}=\{w_1\ \ \phi_{x_1}\ \ \phi_{y_1}\ \ \cdots\ w_4\ \ \phi_{x_4}\ \ \phi_{y_4}\}$, let $\boldsymbol{\psi}$ be the set of Lagrange linear interpolation functions such that

$$\boldsymbol{\psi}=\{\psi_1\ \ \psi_2\ \ \psi_3\ \ \psi_4\}=\{(1-x)(1-y)\ \ (1+x)(1-y)\ \ \times(1+x)(1+y)\ \ (1-x)(1+y)\}.$$

Then, the mass matrix $\mathbf{M}^e$ can be written as $\mathbf{M}^e=h^e\mathbf{M}_1^e+h^{e^3}\mathbf{M}_3^e$ such that

$$\mathbf{M}_1^e=\begin{bmatrix}\mathbf{M}_{1w,w}^e & \mathbf{0} & \mathbf{0}\\ \mathbf{0} & \mathbf{M}_{1\phi x,\phi x}^e & \mathbf{0}\\ \mathbf{0} & \mathbf{0} & \mathbf{M}_{1\phi y,\phi y}^e\end{bmatrix},$$

where

$$\mathbf{M}_{1w}^e=\rho a^2\left[\int_{-1}^{1}\psi_i\psi_j\,\mathrm{d}x\,\mathrm{d}y\right]\quad\text{and}\quad\mathbf{M}_{1\phi x}^e=\mathbf{M}_{1\phi y}^e=\mathbf{0},\qquad i,j=1,2,3,4$$

and

$$\mathbf{M}_3^e=\begin{bmatrix}\mathbf{M}_{3w,w}^e & \mathbf{0} & \mathbf{0}\\ \mathbf{0} & \mathbf{M}_{3\phi x,\phi x}^e & \mathbf{0}\\ \mathbf{0} & \mathbf{0} & \mathbf{M}_{3\phi y,\phi y}^e\end{bmatrix}$$

with

$$\mathbf{M}_{3w,w}^e=\mathbf{0}\quad\text{and}\quad\mathbf{M}_{3\phi x,\phi x}^e=\mathbf{M}_{3\phi y,\phi y}^e=\frac{1}{12}\rho a^2\left[\int_{-1}^{1}\psi_i\psi_j\,\mathrm{d}x\,\mathrm{d}y\right].$$

Also, the stiffness matrix $\mathbf{K}^e$ can be written as $\mathbf{K}^e=h^e\mathbf{K}_1^e+h^{e^3}\mathbf{K}_3^e$ such that

$$\mathbf{K}_1^e=\begin{bmatrix}\mathbf{K}_{1ww}^e & \mathbf{K}_{1w,\phi x}^e & \mathbf{K}_{1w,\phi y}^e\\ & \mathbf{K}_{1\phi x,\phi x}^e & \mathbf{K}_{1\phi x,\phi y}^e\\ sym & & \mathbf{K}_{1\phi y,\phi y}^e\end{bmatrix},$$

where

$$\mathbf{K}_{1w,w}^e=\frac{5E}{12(1+\upsilon)}a^2\left[\int_{-1}^{1}\frac{\partial\psi_i}{\partial x}\frac{\partial\psi_j}{\partial x}+\frac{\partial\psi_i}{\partial y}\frac{\partial\psi_j}{\partial y}\,\mathrm{d}x\,\mathrm{d}y\right],$$

$$\mathbf{K}_{1w,\phi x}^e=\frac{5E}{12(1+\upsilon)}a^2\left[\int_{-1}^{1}\frac{\partial\psi_i}{\partial x}\psi_j\,\mathrm{d}x\,\mathrm{d}y\right],$$

$$\mathbf{K}_{1w,\phi y}^e=\frac{5E}{12(1+\upsilon)}a^2\left[\int_{-1}^{1}\frac{\partial\psi_i}{\partial y}\psi_j\,\mathrm{d}x\,\mathrm{d}y\right],$$

$$\mathbf{K}_{1\phi x,\phi x}^e=\frac{5E}{12(1+\upsilon)}a^2\left[\int_{-1}^{1}\psi_i\psi_j\,\mathrm{d}x\,\mathrm{d}y\right],$$

and

$$\mathbf{K}_{1\phi x,\phi y}^e=\mathbf{0},\quad\mathbf{K}_{1\phi x,\phi y}^e=\frac{5E}{12(1+\upsilon)}a^2\left[\int_{-1}^{1}\psi_i\psi_j\,\mathrm{d}x\,\mathrm{d}y\right].$$

Also,

$$\mathbf{K}_3^e=\begin{bmatrix}\mathbf{K}_{3ww}^e & \mathbf{K}_{3w,\phi x}^e & \mathbf{K}_{3w,\phi y}^e\\ & \mathbf{K}_{3\phi x,\phi x}^e & \mathbf{K}_{3\phi x,\phi y}^e\\ sym & & \mathbf{K}_{3\phi y,\phi y}^e\end{bmatrix}$$

with

$$\mathbf{K}_{3w,w}^e=\mathbf{K}_{3w,\phi x}^e=\mathbf{K}_{3w,\phi y}^e=0,$$

$$\mathbf{K}_{3\phi x,\phi x}^e=\frac{E}{12(1-\upsilon^2)}a^2\left[\int_{-1}^{1}\frac{\partial\psi_i}{\partial x}\frac{\partial\psi_j}{\partial x}+\frac{(1-\upsilon)}{2}\frac{\partial\psi_i}{\partial y}\frac{\partial\psi_j}{\partial y}\,\mathrm{d}x\,\mathrm{d}y\right],$$

$$\mathbf{K}_{3\phi x,\phi y}^e=\frac{E}{12(1-\upsilon^2)}a^2\left[\int_{-1}^{1}\upsilon\frac{\partial\psi_i}{\partial x}\frac{\partial\psi_j}{\partial y}+\frac{(1-\upsilon)}{2}\frac{\partial\psi_i}{\partial y}\frac{\partial\psi_j}{\partial x}\,\mathrm{d}x\,\mathrm{d}y\right],$$

and

$$\mathbf{K}_{3\phi x,\phi y}^e=\frac{E}{12(1-\upsilon^2)}a^2\left[\int_{-1}^{1}\frac{(1-\upsilon)}{2}\frac{\partial\psi_i}{\partial x}\frac{\partial\psi_j}{\partial x}+\frac{\partial\psi_i}{\partial y}\frac{\partial\psi_j}{\partial y}\,\mathrm{d}x\,\mathrm{d}y\right].$$

References

[1] M. Bendsøe, Optimal shape design as a material distribution problem, Struct. Optim. 1 (1989) 193–202.
[2] A. Diáz, M. Bendsøe, Shape optimization of structures for multiple loading situations using a homegenization method, Struct. Optim. 4 (1992) 17–22.
[3] A. Diáz, N. Kikuchi, Solution to shape and topology eigenvalue optimization problems using a homogenization method, Int. J. Numer. Methods Eng. 35 (1992) 1487–1502.
[4] N. Pedersen, Maximization of eigenvalues using topology optimization, Struct. Multidiscip. Optim. 20 (1) (2000) 2–11.
[5] Y. Seo, S. Youn, J. Yeon, S. Chang, J. Yoo, Topology optimization of inner-wall stiffener for critical buckling loads of cylindrical containers, Paper AIAA-2004-4418, in: 10th AIAA/ISSMO Multidisciplinary Analysis and Optimization Conference, Albany, New York, August 30 to September 1, 2004.
[6] S. Cho, S.-H. Ha, C.-Y. Park, Topological shape optimization of power flow problems at high frequencies using level set approach, Int. J. Solids Struct. 43 (2006) 172–192.
[7] D. Jung, H.C. Gea, Design of an energy-absorbing structure using topology optimization with a multimaterial model, J. Struct. Multidiscip. Optim. 32 (3) (2006) 251–257.
[8] O. Sigmund, J. Jensen, Systematic design of phononic band-gap materials and structures by topology optimization, Philos. Trans. R. Soc. London A 361 (2002) 1001–1019.
[9] A. Diáz, A.G. Haddow, L. Ma, Design of band-gap grid structures, Struct. Multidiscip. Optim. 29 (6) (2005) 418–431.
[10] S. Halkjaer, O. Sigmund, J. Jensen, Inverse design of phononic crystals by topology optimization, Z. Kristallogr. 220 (9–10) (2005) 895–905.
[11] S. Halkjaer, O. Sigmund, J. Jensen, Maximizing band gaps in plate structures, Struct Multidiscip. Optim. 32 (2006) 263–275.
[12] J. Reddy, An Introduction to the Finite Element Method, second ed., McGraw-Hill, New York, 1993.
[13] M. Bendsøe, O. Sigmund, Topology Optimization: Theory, Methods and Applications, Springer, Berlin/Heidelberg/New York, 2003.
[14] K. Svanberg, The method of moving asymptotes: a new method for structural optimization, Int. J. Numer. Methods Eng. 24 (1987) 359–373.